

# The role of surface quenching of the singlet delta molecule in a capacitively coupled oxygen discharge

A. Proto<sup>1</sup> and J. T. Gudmundsson<sup>1,2,\*</sup>

<sup>1</sup>*Science Institute, University of Iceland, Dunhaga 3, IS-107 Reykjavik, Iceland*

<sup>2</sup>*Department of Space and Plasma Physics, School of Electrical Engineering and Computer Science, KTH-Royal Institute of Technology, SE-100 44, Stockholm, Sweden*

(Dated: July 10, 2018)

We use the one-dimensional object-oriented particle-in-cell Monte Carlo collision code `oopd1` to explore the influence of the surface quenching of the singlet delta metastable molecule  $O_2(a^1\Delta_g)$  on the electron heating mechanism, and the electron energy probability function (EETF), in a single frequency capacitively coupled oxygen discharge. When operating at low pressure (10 mTorr) varying the surface quenching coefficient in the range 0.00001 – 0.1 has no influence on the electron heating mechanism and electron heating is dominated by drift-ambipolar (DA) heating in the plasma bulk and electron cooling is observed in the sheath regions. As the pressure is increased to 25 mTorr the electron heating becomes a combination of DA-mode and  $\alpha$ -mode heating, and the role of the DA-mode decreases with decreasing surface quenching coefficient. At 50 mTorr electron heating in the sheath region dominates. However, for the highest quenching coefficient there is some contribution from the DA-mode in the plasma bulk, but this contribution decreases to almost zero and pure  $\alpha$ -mode electron heating is observed for a surface quenching coefficient of 0.001 or smaller.

## I. INTRODUCTION

Low pressure radio frequency (rf) driven capacitively coupled plasma (CCP) discharges have been applied in integrated circuit manufacturing for a few decades. Currently the CCPs consist of two parallel electrodes, typically of radius of a few tens of cm, separated by a few cm, and driven by a radio-frequency power supply. In the capacitively coupled discharges a plasma forms between the electrodes, from which it is separated by space charge sheaths. The energy transport mechanism and particle interactions in the plasma-surface interface region play a significant role in the discharge operation. Atomic species recombine to form molecules and metastable species are quenched on the electrode surfaces. Both of these processes influence the discharge operation and can have determining influence on the electronegativity of the discharge and the electron heating mechanisms and thus on the electron kinetics. In turn the electron kinetics dictate the ionization and dissociation processes that maintain the discharge and create the radicals that are desired for materials processing.

When operated at low pressure the electron heating mechanism in a CCP is referred to as being collisionless and is associated with the electron dynamics in the sheath region, a rapid movement of the electrode sheaths or stochastic electron heating [1, 2]. When the electrons interact with the moving sheaths, they can be either cooled (collapsing sheath) or heated (expanding sheath). Energetic electrons can also bounce back and forth between the two sheaths. When they hit the sheath edge during its expansion phase, energy is transferred to the electrons. This electron heating process is referred to as

electron bounce resonance heating (BRH) and can occur for certain combinations of driving frequency and electrode gap [3–7]. The sheath motion and thus the stochastic heating can also be enhanced by self-excited non-linear plasma series resonance (PSR) oscillations [8–11]. Collisionless electron heating via sheath oscillations is commonly referred to as the  $\alpha$ -mode [12]. When the discharge is operated at high applied voltages and pressures secondary electron emission can contribute to or even dominate the ionization, and the operating mode is then referred to as  $\gamma$ -mode [12]. In electronegative discharges large electron density gradients can develop within the rf period which can cause the generation of ambipolar fields along with drift fields, that can accelerate the electrons, a heating mechanism referred to as the drift-ambipolar (DA) mode [13, 14].

The oxygen discharge has been applied in plasma materials processing for decades and its applications include processes such as oxidation or anodization of silicon [15–17], ashing of photoresist [18, 19], and surface modification of polymer films [20–22]. The oxygen discharge is weakly electronegative and the electronegativity depends on the control parameters including pressure and power [23]. At low operating pressure the negative  $O^-$ -ion is the dominant negative ion and it is created almost solely by electron impact dissociative attachment, where the singlet metastables play a significant role [24, 25]. Earlier we have demonstrated how these singlet metastable molecular states influence the electron heating mechanism and thus the electron kinetics in the capacitively coupled oxygen discharge operated at a single frequency of 13.56 MHz [26–29] as well as the ion energy distribution in both single and dual frequency discharges [30]. We have demonstrated that at low pressure (10 mTorr), the electron heating is mainly within the plasma bulk (the electronegative core), and at higher pressures (50 – 500 mTorr) the electron heating occurs mainly in the

---

\*tumi@hi.is

sheath region [27, 28]. When operating at low pressure the electron heating within the discharge is due to combined drift-ambipolar-mode (DA-mode) and  $\alpha$ -mode and at higher pressures the discharge is operated in the  $\alpha$ -mode [31, 32].

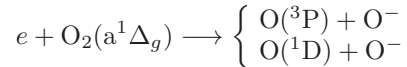
Recent fluid model and PIC/MCC simulation studies have indicated that there are significant changes in the electronegativity and the electron heating mechanism as the quenching coefficient for the  $O_2(a^1\Delta_g)$  on the electrode surfaces is varied [33–35]. Derzsi et al. [34] using a PIC/MCC simulation demonstrate that the  $O_2(a^1\Delta_g)$  density decreases exponentially with increasing quenching coefficient  $\gamma_{wqa}$  in the range  $10^{-4} \leq \gamma_{wqa} \leq 5 \times 10^{-2}$ . In these PIC/MCC simulation studies [34, 35] the  $O_2(a^1\Delta_g)$  density is taken as a fraction of the ground state oxygen molecule  $O_2(X^3\Sigma_g^-)$ . Similarly, using a 1D fluid model, Greb et al. [33] demonstrated that the electronegativity depends strongly on the  $O_2(a^1\Delta_g)$  surface quenching coefficient and argued that increased quenching coefficient leads to decreased  $O_2(a^1\Delta_g)$  density, decreased detachment by the  $O_2(a^1\Delta_g)$  state, and thus higher negative ion density. This is due to the very effective annihilation of the  $O^-$ -ions in the plasma bulk via detachment by the singlet metastable molecules  $O_2(a^1\Delta_g)$ . More recently Gibson and Gans [36] explored the particle dynamics in an oxygen CCP while keeping the  $O_2(a^1\Delta_g)$  as either 16 % or 0.5 % of the ground state density, to create a weakly and highly, electronegative oxygen discharge, respectively. Using a 1D fluid model they demonstrated that oxygen discharges can operate in distinctly different modes dependent upon the  $O_2(a^1\Delta_g)$  density within the discharge. Less is known about the role of the quenching of  $O_2(b^1\Sigma_g)$  on the electrodes.

Here we study how the surface quenching coefficients for the singlet metastable molecules  $O_2(a^1\Delta_g)$  influence the electron heating processes, the electron energy probability function (EPPF), the effective electron temperature, in the single frequency voltage driven capacitively coupled oxygen discharge by means of numerical simulation, for a fixed discharge voltage, while the discharge pressure is varied from 10 to 50 mTorr. The simulation parameters and the cases explored are defined in section II, where we give an overview of the known surface quenching coefficients for the singlet metastable molecules on various surfaces and determine the partial pressures of the neutral background species using a global model. The results of the PIC/MCC simulations, the various electron heating modes observed for the various combinations of surface quenching coefficients and operating pressures, are discussed in section III. Finally, concluding remarks are given in section IV.

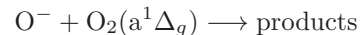
## II. THE SIMULATION

The one-dimensional object-oriented particle-in-cell Monte Carlo collision (PIC/MCC) code `oopd1` [37, 38] is here applied to a capacitively coupled oxygen discharge.

In 1d-3v PIC codes, like `oopd1`, the model system has one spatial dimension and three velocity components. In our earlier work we added oxygen atoms in the ground state  $O(^3P)$  and ions of the oxygen atom  $O^+$  and the relevant reactions to the `oopd1` discharge model [39]. Later we added the singlet metastable molecule  $O_2(a^1\Delta_g)$ , the metastable oxygen atom  $O(^1D)$  [26], and the singlet metastable molecule  $O_2(b^1\Sigma_g^+)$  [28], along with energy dependent secondary electron emission coefficients for oxygen ions and neutrals as they bombard the electrodes [28]. For this current work the discharge model contains nine species: electrons, the ground state neutrals  $O(^3P)$  and  $O_2(X^3\Sigma_g^-)$ , the negative ions  $O^-$ , the positive ions  $O^+$  and  $O_2^+$ , and the metastables  $O(^1D)$ ,  $O_2(a^1\Delta_g)$  and  $O_2(b^1\Sigma_g^+)$ . The full oxygen reaction set and the cross sections used have been discussed in our earlier works and will not be repeated here [26, 28, 39]. However, as the role of the singlet metastable oxygen molecule  $O_2(a^1\Delta_g)$  is being explored two important reactions are mentioned here (see further discussion in Gudmundsson and Lieberman [26]). It is known from global model studies [24] that dissociative attachment of the oxygen molecule is almost the sole source of  $O^-$ -ions in the discharge and the metastable oxygen molecules play a major role. In particular dissociative attachment from the metastable oxygen molecule  $O_2(a^1\Delta_g)$  can be the dominant path for the creation of negative ion  $O^-$  through



Lower pressure and thus higher effective electron temperature promotes the creation of the negative ion  $O^-$ . The metastable molecule  $O_2(a^1\Delta_g)$  also contributes significantly to the loss of the negative ion  $O^-$ -ion through the detachment process



while detachment by the oxygen molecule in the ground state is negligible. Here we use the rate coefficient measured at 400 K of  $1.5 \times 10^{-16}$  m<sup>3</sup>/s by Midey et al. [40] to estimate the cross section by assuming a Maxwellian velocity distribution of the particles. The cross section is allowed to fall as  $1/\sqrt{\mathcal{E}}$  to 184 meV and then take a fixed value of  $5.75 \times 10^{-20}$  m<sup>2</sup>. Also we assume that the detachment by the metastable molecule  $O_2(a^1\Delta_g)$  leads to the formation of  $O(^3P) + O_2(X^3\Sigma_g^-) + e$ , instead of  $O_3 + e$  and  $O + O_2^-$ . Increased discharge pressure thus promotes the loss of the negative ion  $O^-$ .

We assume a symmetric capacitively coupled discharge where one of the electrodes is driven by an rf voltage

$$V(t) = V_0 \sin(2\pi ft) \quad (1)$$

while the other is grounded. Here  $V_0$  is the voltage amplitude,  $f$  the driving frequency, and  $t$  is the time. For this current study we assume the discharge to be operated with voltage amplitude of  $V_0 = 222$  V with an

electrode separation of 4.5 cm and a capacitor of 1 F in series with the voltage source, while the surface quenching coefficient for the singlet delta metastable  $O_2(a^1\Delta_g)$  and discharge pressure is varied. These are the same parameters as assumed in our earlier work using `oopd1` [26, 28, 29, 32, 39] and by Lichtenberg *et al.* [41] using the `xpdp1` code. The discharge electrode separation is assumed to be small compared to the electrode diameter so that the discharge can be treated as one dimensional. We assume 10.25 cm diameter electrodes in order to determine the absorbed power and set the discharge volume for the global model calculations, discussed in section II C. The time step  $\Delta t$  and the grid spacing  $\Delta x$  resolve the electron plasma frequency and the electron Debye length of the low-energy electrons, respectively, according to  $\omega_{pe}\Delta t < 0.2$ , where  $\omega_{pe}$  is the electron plasma frequency, and the simulation grid is uniform and consists of 1000 cells. The electron time step is  $3.68 \times 10^{-11}$  s. The simulation was run for  $5.5 \times 10^6$  time steps or 2750 rf cycles. It takes roughly 1700 rf cycles to reach equilibrium for all particles and the time averaged plasma parameters shown, such as the densities, the electron heating rate, and the effective electron temperature, are averages over 1000 rf cycles. All particle interactions are treated by the Monte Carlo method with a null-collision scheme [42]. For the heavy particles we use a sub-cycling and the heavy particles are advanced every 16 electron time steps and we assume that the initial density profiles are parabolic [43].

The kinetics of the charged particles (electrons,  $O_2^+$ -ions,  $O^+$ -ions and  $O^-$ -ions) was followed for all energies. Since the neutral gas density is much higher than the densities of charged species, the neutral species at thermal energies (below a certain cut-off energy) are treated as a background with fixed density and temperature and maintained uniformly in space. These neutral background species are assumed to have a Maxwellian velocity distribution at the gas temperature (here  $T_n = 26$  mV). The kinetics of the neutrals are followed when their energy exceeds a preset energy threshold value. The energy threshold values used here for the various neutral species are listed in Table I. Due to recombination of atomic oxygen and quenching of metastable atoms and molecules on the electrode surfaces there is a drop in the high energy (energy above the threshold value) atomic oxygen density and increase in the high energy oxygen molecule densities next to the electrodes as shown in our earlier work [28]. Thus assuming uniformity of the background gas is thus somewhat unrealistic assumption.

The ratio of the number of physical particles to computational particles, the particle weight, is also listed in Table I for all the neutral species. Note that in `oopd1` the particles can have different weights [44, 45] and the collisions among particles with different weights is implemented in `oopd1` following the method suggested by Miller and Combi [46].

In our earlier studies we have used fixed partial pressure for each of the neutral species as we have varied

TABLE I: The parameters of the simulation, the particle weight, and the energy threshold above which dynamics of the neutral particles are followed.

Species	particle energy	
	weight	threshold [meV]
$O_2(X^3\Sigma_g^-)$	$5 \times 10^7$	500
$O_2(a^1\Delta_g)$	$5 \times 10^6$	100
$O_2(b^1\Sigma_g)$	$5 \times 10^6$	100
$O(^3P)$	$5 \times 10^7$	500
$O(^1D)$	$5 \times 10^7$	50
$O_2^+$	$10^7$	-
$O^+$	$10^6$	-
$O^-$	$5 \times 10^7$	-
e	$1 \times 10^7$	-

the pressure [27], the driving voltage amplitude [31], and the driving frequency [32]. Here we take a different approach and calculate the partial pressure for each combination of pressure and surface quenching coefficient using a global (volume averaged) model as discussed in section II C. The two electrodes are assumed to be identical, and the surface coefficients, surface recombination and surface quenching, are kept the same at both electrodes. We neglect the reflection of electrons from the electrodes.

### A. Wall recombination coefficients

As a neutral species hits the electrode it returns as a thermal particle with a given probability and atoms can recombine to form a thermal molecule with the given probability. The wall recombination coefficient for the neutral atoms in ground state  $O(^3P)$  is taken to be 0.5 as measured by Booth and Sadeghi [47] for a pure oxygen discharge in a stainless steel reactor at 2 mTorr. As the oxygen atom  $O(^3P)$  hits the electrode we assume that half of the atoms are reflected as  $O(^3P)$  at room temperature and the other half recombines to form the ground state oxygen molecule  $O_2(X^3\Sigma_g^-)$  at room temperature. Note that this is a rough assumption as it is known that the wall recombination coefficient drops significantly with increased pressure [24]. This could lead to underestimation of the atomic oxygen density. However, the atomic oxygen density is low and is expected to decrease with increased pressure so this is not expected to have a significant influence on the results reported here. Similarly, as the metastable atom  $O(^1D)$  hits the electrode we assume that half of the atoms are quenched to form  $O(^3P)$  and the other half recombines to form the ground state oxygen molecule  $O_2(X^3\Sigma_g^-)$  at room temperature.

## B. Wall quenching coefficients

It is difficult to determine an actual value for the surface quenching coefficients of the singlet metastables on the electrode surfaces either experimentally or theoretically. In general we would expect that the quenching probability for any excited species hitting the electrodes to depend not only on the species itself, but also on the surface material, the surface temperature, and the actual surface condition, such as surface roughness and contamination, which can vary substantially. Indeed it has been pointed out by Du et al. [48] that the quenching probability of  $O_2(a^1\Delta_g)$  increases with both the duration of the exposure to and the concentration of  $O_2(a^1\Delta_g)$ . The values for the measured wall quenching coefficient, found in the literature, for  $O_2(a^1\Delta_g)$  and  $O_2(b^1\Sigma_g^+)$  on various surfaces are listed in Table II. All of the values listed in Table II were measured at room temperature. We note that the listed values span a few orders of magnitude and depend on the surface material. Furthermore, we note that the measured values also vary by orders of magnitude for the same materials. We also note that the quenching probability for  $O_2(b^1\Sigma_g^+)$  is in general significantly higher than for  $O_2(a^1\Delta_g)$ . In our earlier studies [25, 27–29, 32] we have used a quenching coefficients for the singlet metastable  $O_2(a^1\Delta_g)$  on the electrode surface of  $\gamma_{wqa} = 0.007$ , estimated by Sharpless and Slanger for iron [49]. As the measured wall quenching probability for  $O_2(a^1\Delta_g)$  on aluminum is lower than for iron, as seen in Table II, we would expect that aluminum electrodes would therefore lead to higher singlet metastable densities and lower electronegativity. In these studies we assumed the quenching coefficient for  $O_2(b^1\Sigma_g^+)$  to be  $\gamma_{wqb} = 0.1$ , an assumed value, based on the suggestion that the quenching coefficient for the  $b^1\Sigma_g^+$  state is about two orders of magnitude larger than for the  $a^1\Delta_g$  state [50]. We will use this value for the surface quenching coefficient of  $O_2(b^1\Sigma_g^+)$  in this current study. We are aware that this may be overestimation based on the values listed in Table II. We have seen in global model studies that wall quenching can be the main loss mechanism for the singlet metastable state  $O_2(b^1\Sigma_g^+)$  [25]. Gordiets et al. [51] and Kutasi et al. [52] use wall quenching coefficient for  $O_2(a^1\Delta_g)$  of  $2 \times 10^{-5}$  and for  $O_2(b^1\Sigma_g^+)$  of  $2 \times 10^{-2}$  for a quartz tube in their models of flowing  $N_2/O_2$  dc glow discharge and Ar/ $O_2$  surface-wave microwave discharge, respectively. By comparing the 1D fluid simulations to phase and space resolved optical emission (PROES) measurements Greb et al. [53] determine the wall quenching coefficient for  $O_2(a^1\Delta_g)$  to be  $1 \times 10^{-5}$  for stainless steel and  $3 \times 10^{-3}$  for teflon. A comparison of PIC/MCC simulation with experimental findings using PROES for a CCP with aluminum electrodes and electrode spacing of 2.5 cm suggests a wall quenching coefficient of 0.006 [35]. Due to the fact that the measured surface quenching coefficients for  $O_2(a^1\Delta_g)$  vary a few orders of magnitude from roughly  $10^{-5}$  to a few times  $10^{-2}$  we allow the surface quenching coefficients for  $O_2(a^1\Delta_g)$  to vary

TABLE II: Overview of the measured wall quenching coefficients for the singlet metastables  $O_2(a^1\Delta_g)$  and  $O_2(b^1\Sigma_g^+)$  that can be found in the literature. All of the values listed were measured at room temperature.

Surface	$O_2(a^1\Delta_g)$	Ref.	$O_2(b^1\Sigma_g^+)$	Ref.
	$\gamma_{wqa}$		$\gamma_{wqb}$	
Pyrex	$(3.1 \pm 0.2) \times 10^{-5}$	[54]	$2 \times 10^{-3}$	[55]
	$1.3 \times 10^{-5}$	[56]	$2.2 \times 10^{-3}$	[57]
	$2.1 \times 10^{-5}$	[58]	$1 \times 10^{-2}$	[59]
	$4.3 \times 10^{-5}$	[60]		
Teflon	$< 10^{-3}$	[49]	$4.5 \times 10^{-3}$	[55]
Fe	$7 \times 10^{-3}$	[49]		
	$4.4 \times 10^{-3}$	[61]		
Cu	$1.4 \times 10^{-2}$	[49]	$1.0 \times 10^{-2}$	[55]
	$8.5 \times 10^{-4}$	[61]		
	$2.9 \times 10^{-4}$	[54]		
Ni	$1.15 - 1.43 \times 10^{-3}$	[48]		
	$2.7 \times 10^{-3}$	[61]	$2.6 \times 10^{-2}$	[55]
	$1.1 \times 10^{-2}$	[49]		
	$(3.1 \pm 0.2) \times 10^{-4}$	[54]		
Monel (Cu/Ni)	$0.6 - 1.0 \times 10^{-3}$	[48]		
	$(2.8 \pm 0.2) \times 10^{-4}$	[54]		
Al	$1.2 \times 10^{-2}$	[49]		
	$< 10^{-3}$	[49]		
Pt	$5.9 \times 10^{-5}$	[61]		
	$1 \times 10^{-2}$	[49]		
Ti	$4.0 \times 10^{-4}$	[61]		
	$6.5 \times 10^{-5}$	[61]		
Ag	$< 10^{-3}$	[49]		
	$1.1 \times 10^{-2}$	[61]		
Si	$7.3 \times 10^{-4}$	[61]		
Graphite	$3 \times 10^{-3}$	[49]		

in the range 0.00001 – 0.1 as we explore the how it influences the electron heating processes. The lowest value of 0.00001 corresponds to pyrex or aluminum and values of 0.01 correspond to Pt or Ag electrodes.

## C. Global model – partial pressures

To determine the partial pressures of the background thermal neutral species we applied a global (volume averaged) model of the oxygen discharge. The global model used is discussed in detail by Thorsteinsson and Gudmundsson [62] but 32 additional reactions have been added to improve the treatment of  $O_2(b^1\Sigma_g^+)$ ,  $O_3$ , and  $O_2^-$  [63], and in order to make the oxygen reaction set as detailed as the one discussed by Toneli et al. [25]. We explored the partial pressures at 10, 25 and 50 mTorr and the total absorbed power was found to be 1.8 W after iteration between the oopd1 simulations and the

TABLE III: The partial pressures of the thermal neutrals at 10, 25 and 50 mTorr for different wall quenching coefficients of the singlet metastable molecule  $O_2(a^1\Delta_g)$  calculated by a global (volume averaged) model.

$\gamma_{wqa}$	$O_2(X^3\Sigma_g^-)$	$O_2(a^1\Delta_g)$	$O_2(b^1\Sigma_g)$	$O(^3P)$
10 mTorr				
$10^{-1}$	0.9926	0.0022	0.0015	0.0015
$10^{-2}$	0.9825	0.0124	0.0016	0.0009
$10^{-3}$	0.9717	0.0240	0.0018	0.0007
$10^{-4}$	0.9684	0.0265	0.0018	0.0015
$10^{-5}$	0.9681	0.0268	0.0018	0.0015
25 mTorr				
$10^{-1}$	0.9918	0.0018	0.0012	0.0006
$10^{-2}$	0.9847	0.0105	0.0015	0.0007
$10^{-3}$	0.9667	0.0290	0.0019	0.0007
$10^{-4}$	0.9607	0.0350	0.0019	0.0007
$10^{-5}$	0.9600	0.0357	0.0020	0.0007
50 mTorr				
$10^{-1}$	0.9895	0.0013	0.001	0.0003
$10^{-2}$	0.9883	0.0054	0.0015	0.0004
$10^{-3}$	0.9791	0.0161	0.0020	0.0004
$10^{-4}$	0.9739	0.0215	0.0022	0.0004
$10^{-5}$	0.9732	0.0223	0.0022	0.0004

global model. We assume a cylindrical discharge of diameter 10.25 cm and length 4.5 cm. We vary the surface quenching coefficient for the singlet metastable molecule  $O_2(a^1\Delta_g)$  in the range  $\gamma_{wqa} = 0.00001 - 0.1$  while the surface quenching coefficient for the singlet metastable molecule  $O_2(b^1\Sigma_g)$  is kept constant  $\gamma_{wqb} = 0.1$ . The fractional densities found by the global model calculations involving the neutrals  $O_2(X^3\Sigma_g^-)$ ,  $O(^3P)$ ,  $O_2(a^1\Delta_g)$  and  $O_2(b^1\Sigma_g)$  are listed in Table III. These values are used as input for the simulation in the particle-in-cell Monte Carlo collision (PIC/MCC) code `oopd1` as the partial pressure of the neutral background gas. Note that not all the neutrals considered in the global model calculations are shown in the table. We see that the partial pressure of the singlet metastable molecule  $O_2(a^1\Delta_g)$  increases with decreasing surface quenching coefficient and takes its highest value at 25 mTorr for the lowest surface quenching coefficient. The partial pressure of  $O_2(b^1\Sigma_g)$  is always much smaller, maybe due to too large surface quenching coefficient.

### III. RESULTS AND DISCUSSION

Figures 1 show the spatio temporal behaviour of the electron power absorption as the surface quenching coefficient for the singlet metastable molecule  $O_2(a^1\Delta_g)$  is varied in the range 0.00001 - 0.1, for pressures of 10 mTorr (left column), 25 mTorr (center column) and 50 mTorr (right column). The electron power absorption is calculated as  $\mathbf{J}_e \cdot \mathbf{E}$ , where  $\mathbf{J}_e$  and  $\mathbf{E}$  are the spatially and temporally varying electron current density and electric field, respectively. For each of the figures the abscissa covers the whole inter-electrode gap, from the powered electrode on the left hand side to the grounded electrode on the right hand side. Similarly the ordinate covers the full rf cycle. As displayed in Figure 1 left column, for low pressure (10 mTorr), the change in the quenching coefficient  $\gamma_{wqa}$  does not alter the heating mechanism, which is a combination of a drift ambipolar (DA) heating in the bulk plasma and stochastic heating due to the sheath oscillation ( $\alpha$ -mode). As the operating pressure is raised to 25 mTorr (see Figure 1 center column) varying the quenching coefficients clearly has an influence on the heating mechanism. For a high quenching coefficient the electron heating is a combination of DA- and  $\alpha$ -mode, as seen in Figure 1 center column (e), similar to what is seen at 10 mTorr independent of the quenching coefficient (Figure 1 left column (a) - (e)). As the quenching coefficient is lowered the bulk heating decreases and stochastic heating in the sheath region becomes more prominent, as seen in Figures 1 center column (d) - (a). At 50 mTorr we still see some bulk heating for the highest quenching coefficients (Figures 1 right column (e) - (d)) but for low quenching coefficients there is no electron heating observed in the plasma bulk (Figures 1 right column (c) - (a)) and pure  $\alpha$ -mode is observed. Figure 2 shows the time averaged electron heating profile between the electrodes  $\langle \mathbf{J}_e \cdot \mathbf{E} \rangle$ . We see in Figure 2 (a) that at 10 mTorr almost all the electron heating occurs in the plasma bulk (the electronegative core) and the electron heating profile is almost independent of the surface quenching coefficient for the singlet metastable molecule  $O_2(a^1\Delta_g)$ . In the sheath regions the time averaged  $\langle \mathbf{J}_e \cdot \mathbf{E} \rangle$  value indicates electron cooling. This can occur in the sheath regions as the DA-heating in the bulk maintains the discharge. At 25 mTorr for high surface quenching coefficient the electron heating in the plasma bulk region dominates as seen in Figure 2 (b). As the surface quenching coefficient for the singlet metastable molecule  $O_2(a^1\Delta_g)$  decreases the electron heating in the bulk region decreases and the heating in the sheath regions increases. For surface quenching coefficient in the range 0.001 - 0.00001 the time averaged heating profile remains roughly the same, electron heating occurs both in the bulk and in the sheath regions, and a combination of DA- and  $\alpha$ -mode is observed. When operating at 50 mTorr electron heating in the sheath region dominates as seen in Figure 2 (c). Only for the highest surface quenching coefficients 0.1 and 0.01 there is some electron heating observed in the

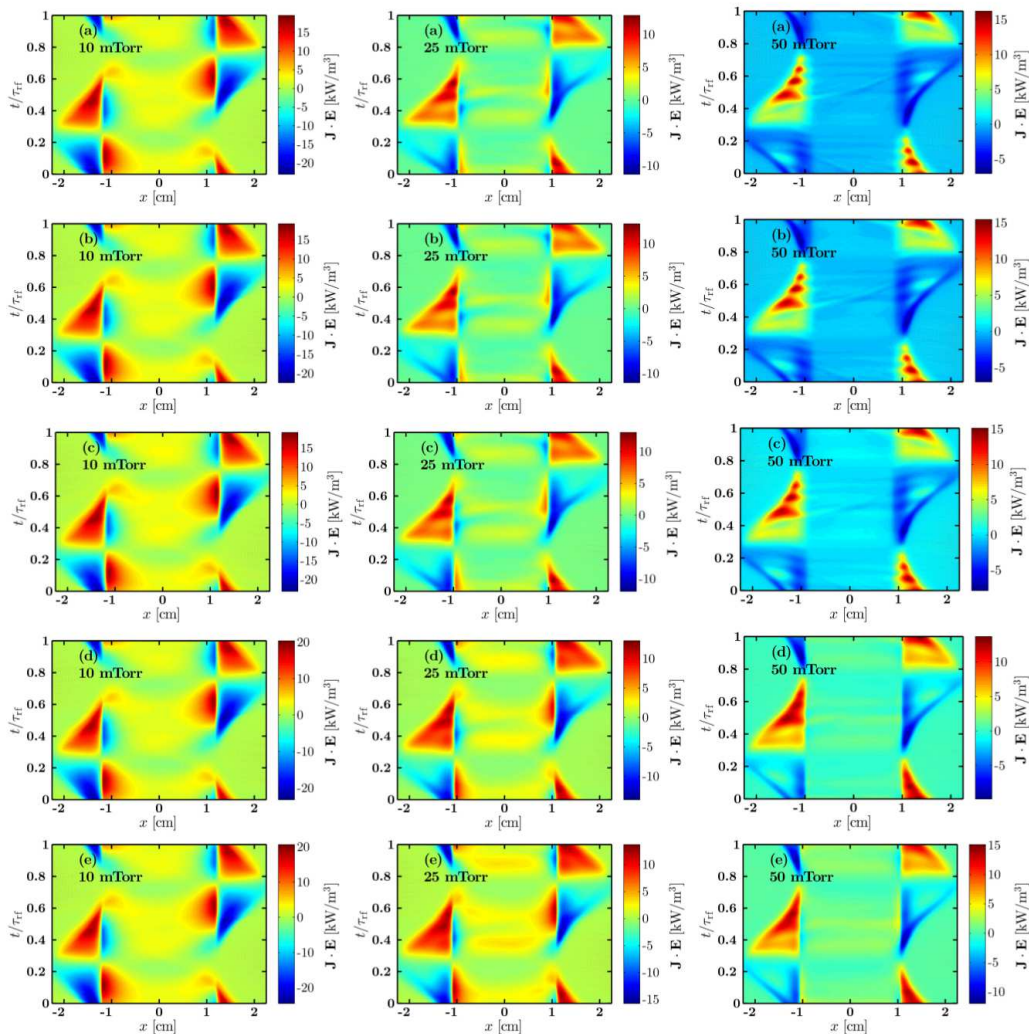


FIG. 1: The spatio-temporal behaviour of the electron power absorption at 10 mTorr (left column), 25 mTorr (center column) and 50 mTorr (right column) for surface quenching coefficient for the singlet metastable molecule  $O_2(a^1\Delta_g)$  as (a)  $\gamma_{wqa} = 0.00001$ , (b)  $\gamma_{wqa} = 0.0001$ , (c)  $\gamma_{wqa} = 0.001$ , (d)  $\gamma_{wqa} = 0.01$  and (e)  $\gamma_{wqa} = 0.1$  for a parallel plate capacitively coupled oxygen discharge with electrode separation of 4.5 cm driven by a 222 V voltage source at driving frequency of 13.56 MHz.

bulk region. For surface quenching coefficients  $< 0.001$  there is almost no electron heating in the bulk region at 50 mTorr. Furthermore, at the higher pressures 25 mTorr and 50 mTorr, the more the quenching coefficient is raised, the more the power absorption in the bulk is increased. Also, when the power absorption in the bulk increases, the power absorption in the sheath regions decreases. High frequency oscillations in the electron power absorption density adjacent to the expanding sheath edge are seen at 25 and 50 mTorr and become more clear as the pressure is increased and the surface quenching coefficient is decreased. These oscillations are a beam-plasma instability at the electron plasma frequency, due to an electron-electron two-stream instability between the bulk electrons and electrons accelerated by the moving sheath

[11, 64].

In order to explore further the observed transition we plot the time averaged center electronegativity as a function of the surface quenching coefficient for the singlet metastable molecule  $O_2(a^1\Delta_g)$  in Figure 3. At 10 mTorr the discharge is the most electronegative and the least electronegative at 50 mTorr. At 10 mTorr the electronegativity does not vary much when the surface quenching coefficient is varied. The electronegativity is high, in the range 107 – 114, as the surface quenching coefficient is decreased from 0.1 to 0.00001. At 25 and 50 mTorr an increase in the electronegativity is observed with increasing surface quenching coefficient. At 25 mTorr the electronegativity increases from 61 to 90, and at 50 mTorr the electronegativity increases from 13 to 52 as the sur-

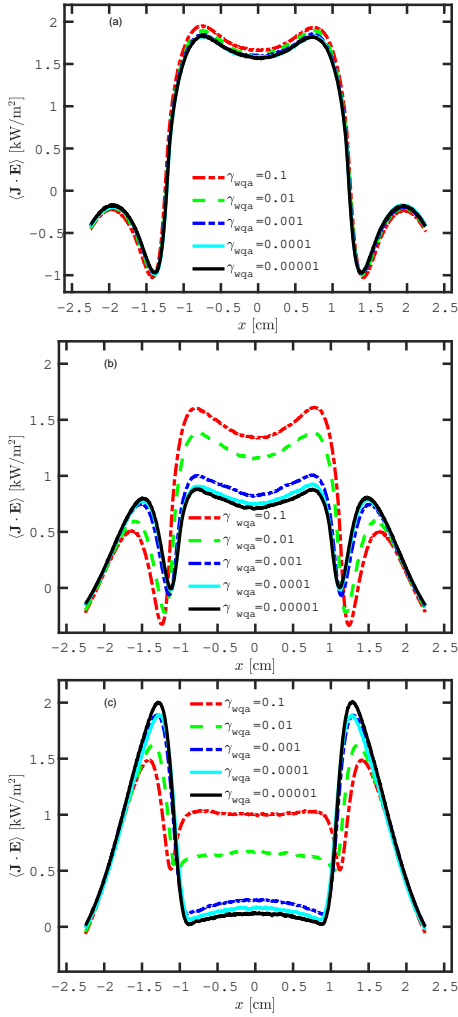


FIG. 2: The time averaged electron heating profile for a parallel plate capacitively coupled oxygen discharge at (a) 10 mTorr, (b) 25 mTorr, and (c) 50 mTorr, with a gap separation of 4.5 cm driven by a 222 V voltage source at driving frequency of 13.56 MHz.

face quenching coefficient is increased. This is related to the fact that, when the surface quenching coefficient is increased, the number of singlet delta metastable molecules  $O_2(a^1\Delta_g)$  decreases, the negative ion density increases, and the electronegativity increases. This also means, as has been pointed out by others [33–35], that the surface quenching coefficient dictates the electronegativity of the oxygen discharge. We note that the electronegativity in this current study is somewhat larger than we have reported in our earlier works [28, 32], particularly at the higher pressures. This is due to the fact that the density of the singlet metastable molecule  $O_2(a^1\Delta_g)$  is somewhat lower in this current study and the density of the the singlet metastable molecule  $O_2(b^1\Sigma_g)$  is significantly lower than assumed in the earlier studies. These are the results of the improved global model calculations as dis-

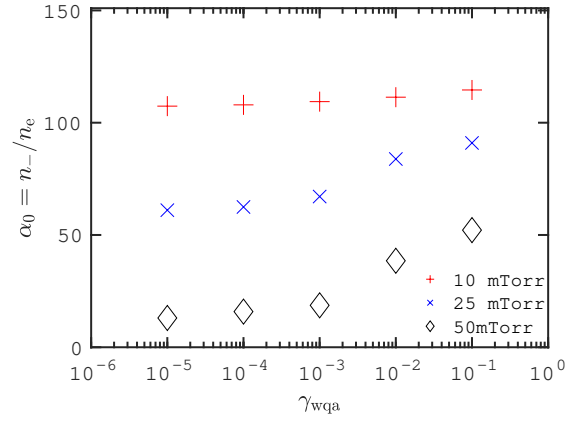


FIG. 3: The electronegativity in the discharge center ( $\alpha_0$ ) as a function of the quenching coefficient of the singlet metastable molecule  $O_2(a^1\Delta_g)$  for a parallel plate capacitively coupled oxygen discharge with a gap separation of 4.5 cm driven by a 222 V voltage source at driving frequency of 13.56 MHz.

cussed in section II C. A few measurements of the electronegativity in capacitively coupled oxygen discharges have been reported. Berezhnoj et al. [65] report a value of around 10 in a symmetric capacitively coupled oxygen discharge with stainless steel electrodes operated at 45 mTorr with electrode spacing of 6 cm. At 50 mTorr we find electronegativity of 13 for  $\gamma_{wqa} = 10^{-5}$  and 18.7 for  $\gamma_{wqa} = 10^{-3}$ . Similarly, Katsch et al. [66] estimated the electronegativity in the discharge center of a capacitively coupled oxygen discharge, with aluminum electrodes with 2.54 cm separation, to be roughly 2 at 103 mTorr and 150 V and to fall below unity at 280 V. We would expect the electronegativity to decrease for aluminum electrodes and higher pressure. For higher pressures Küllig et al. [67] reported electronegativity of 5 – 6 at 225 mTorr in an asymmetric capacitively coupled discharge with stainless steel electrodes and Kaga et al. [68] measured center electronegativity of 7.4 – 11.6 at 100 mTorr and 10.8 – 18.6 at 500 mTorr with aluminum electrodes with spacing of 6 cm.

The time averaged electron density profile is shown in Figure 4. The center electron density at 10 mTorr is  $8.6 \times 10^{13} \text{ m}^{-3}$  and is roughly independent of the surface quenching coefficient as seen in Figure 4 (a). The electron density profile is flat within the plasma bulk with a peak close to the sheath edge. At 25 mTorr the center electron density is  $1.25 \times 10^{14} \text{ m}^{-3}$  for  $\gamma_{wqa} = 0.1$  and increases slightly with decreasing quenching coefficient or to  $1.57 \times 10^{14} \text{ m}^{-3}$  for  $\gamma_{wqa} = 0.00001$ . The electron density profile is flat within the plasma bulk and an increase in the density is observed close to the sheath edge. At 50 mTorr the electron density is  $2.4 \times 10^{14} \text{ m}^{-3}$  for  $\gamma_{wqa} = 0.1$  and increases with decreasing quenching coefficient to  $7.7 \times 10^{14} \text{ m}^{-3}$  for  $\gamma_{wqa} = 0.00001$ . The electron density profile is flat within the plasma bulk and

here no increase (or a peak) is observed at the sheath edge. Kechkar et al. [69] explored experimentally slightly asymmetric capacitively couple oxygen discharge operated at 13.56 MHz, and report electron density in the range  $10^{15} - 7 \times 10^{16} \text{ m}^{-3}$  for a discharge operated at 100 mTorr while the power is varied in the range 30 – 600 W. When operating low power of 30 W, in what they refer to as the  $\alpha$ -mode, the electron density is in the range  $6 \times 10^{14} - 1.6 \times 10^{15} \text{ m}^{-3}$ , increasing with increasing pressure from 10 – 50 mTorr. These values measured at low power of 30 W and in the pressure range 10 – 50 mTorr are very similar to the simulated electron density values reported here. Also Katsch et al. [66] report electron density of  $3 \times 10^{14} \text{ m}^{-3}$  at 150 V and  $1.4 \times 10^{15}$  at 280 V when operating oxygen discharge at 100 mTorr and Berezhnoj et al. [65] report electron density of  $1.1 \times 10^{14} \text{ m}^{-3}$  in a symmetric capacitively coupled oxygen discharge with stainless steel electrodes operated at 45 mTorr with electrode spacing of 6 cm, and current density of  $J = 0.31 \text{ mA/cm}^2$ .

Figure 5 shows the electric field profile in the plasma bulk for the various quenching coefficients at a fixed time slice  $t/\tau_{\text{rf}} = 0.5$ . Note that these curves are not time averaged. At 10 mTorr there is a strong electric field gradient in the bulk region and the electric field strength and profile is independent of the surface quenching coefficient as seen in Figure 5 (a). The electric field is almost flat and takes its lowest absolute value in the center of the electronegative core, while it assumes strong values as the sheath region is approached. The shape of the electric field profile is similar to the one predicted by the simple model of Schulze et al. [13]. The resulting electric field is a combination of a drift field and an ambipolar field. The drift electric field is due to low bulk conductivity or low electron density. We have seen in Figure 4 that the electron density is very low indeed. The peak in the electric field at the sheath edge is mainly caused by a local maximum of the electron density at the sheath edge and the corresponding high value of  $\partial n_e/\partial x$  on the plasma bulk side of this maximum. At this location diffusion directs the electrons into the plasma bulk, while positive ions flow continuously toward the electrode. This generates an ambipolar field, that couples electron and positive ion motion and accelerates electrons towards the electrode. At 25 mTorr and 50 mTorr (Figure 5 (b) and Figure 5 (c)) important changes are observed. For both the pressures considered, the higher the quenching coefficient, the higher is the electric field peak in the sheath region. There is clearly a transition from DA- $\alpha$ -mode to  $\alpha$ -mode when increasing the operating pressure from 25 mTorr to 50 mTorr. At 50 mTorr and low quenching coefficient the electric field is flat and no peaks are observed on the plasma bulk side of the sheath edge. Transitions between the DA-mode and the  $\alpha$ -mode have been demonstrated by both simulations and experiments on  $\text{CF}_4$  discharges [13, 70] where by increasing the operating pressure at a fixed applied voltage, a transition from the  $\alpha$ -mode to the DA-mode is induced. Note that

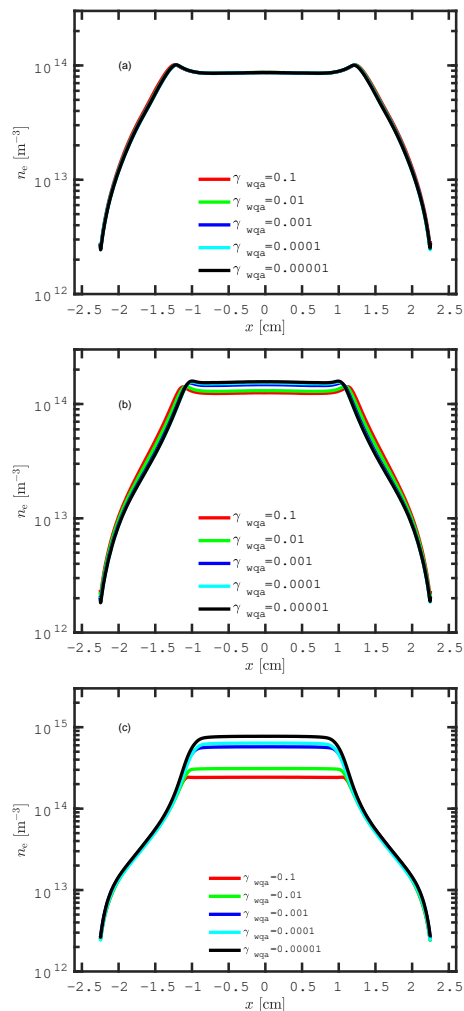


FIG. 4: The electron density profile for a parallel plate capacitively coupled oxygen discharge at (a) 10 mTorr, (b) 25 mTorr, and (c) 50 mTorr, with a gap separation of 4.5 cm driven by a 222 V voltage source at driving frequency of 13.56 MHz.

the  $\text{CF}_4$  discharge is weakly electronegative at 75 mTorr while it is strongly electronegative at 600 mTorr [14]. Also by increasing the voltage at a fixed pressure, a transition from the DA-mode to the  $\alpha$ -mode is observed in a  $\text{CF}_4$  discharge [13]. Oxygen behaves in the opposite way, by increasing the pressure at a given voltage a transition from the DA- $\alpha$ -mode to the  $\alpha$ -mode is observed in the oxygen discharge [31]. This is a similar to the transition reported by Derzsi et al. [35] which observe an operation mode transition from DA- $\alpha$ -mode to  $\alpha$ -mode in an oxygen discharge as harmonics are added to the voltage waveforms for 10 and 15 MHz driving frequency, which also coincides with a strong decrease in the electronegativity.

The evolution of the electron energy probability function (EEPF) in the discharge center with surface quench-



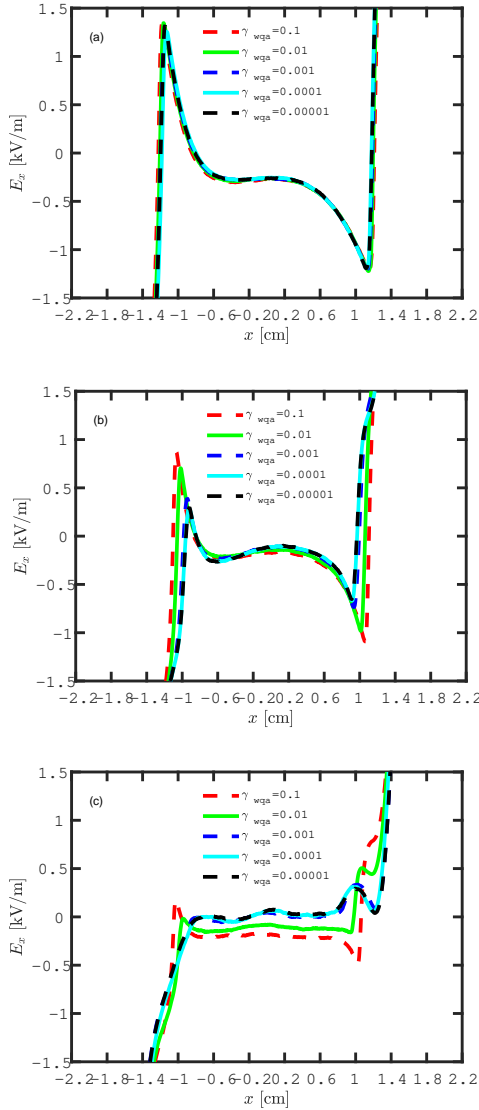


FIG. 5: The electric field in the bulk region at  $t/\tau_{rf} = 0.5$  for a parallel plate capacitively coupled oxygen discharge at (a) 10 mTorr, (b) 25 mTorr, and (c) 50 mTorr with a gap separation of 4.5 cm driven by a 222 V voltage source at driving frequency of 13.56 MHz.

ing coefficient  $\gamma_{wqa}$  is shown in Figure 6. At the lower pressures 10 mTorr and 25 mTorr (Figures 6 (a) and (b)) the EEPF curves outward for every quenching coefficient value. This is due to the significant contribution of the DA-mode to the bulk electron heating as clearly seen in Figures 2 (a) and (b) for 10 and 25 mTorr, respectively. At the higher pressure of 50 mTorr the EEPF still curves outward for the highest quenching coefficients (as there is DA-heating present) but it transitions to curve inward (bi-Maxwellian) for the lowest quenching coefficients. The bi-Maxwellian shape of the EEPF in CCPs is commonly associated with predominant sheath

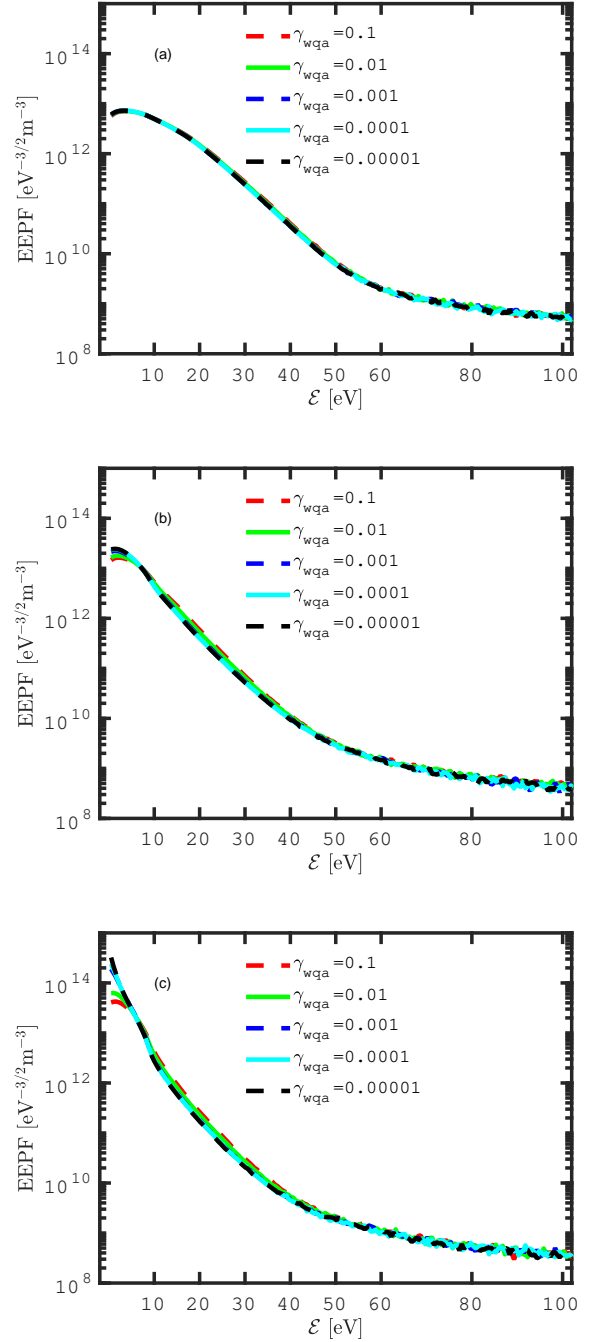


FIG. 6: The electron energy probability function (EEPF) in the discharge center for a parallel plate capacitively coupled oxygen discharge at (a) 10 mTorr, (b) 25 mTorr, and (c) 50 mTorr with a gap separation of 4.5 cm driven by a 222 V voltage source at driving frequency of 13.56 MHz.

heating ( $\alpha$ -mode). The low energy electron population represents electrons confined in the bulk plasma by an ambipolar potential, which are only weakly heated by the rf field, while the high energy population participates in the sheath heating. So the population of low energy electrons is high, as the bulk heating mechanism is weak. At 50 mTorr the electron probability function shows the highest value for low surface quenching, i.e. it has transitioned to become a bi-Maxwellian, that is when the sheath heating mechanism predominates, as was seen in Figure 1 right column (a) – (c), where the bulk heating is almost absent.

#### IV. CONCLUSION

The one-dimensional object-oriented particle-in-cell Monte Carlo collision code `oopd1` was applied to explore the evolution of the electron heating mechanism and the EEPF in a capacitively coupled oxygen discharge while the wall quenching probability of the single metastable molecule  $O_2(a^1\Delta_g)$  is varied. We find that at low pressure (10 mTorr) the surface quenching coefficient has no influence on the electron heating mechanism and electron heating is dominated by drift-ambipolar heating in the plasma bulk and electron cooling is observed in the sheath region. At 25 mTorr the electron heating exhibits

a combination of DA-mode and  $\alpha$ -mode. For the highest quenching coefficient the DA-mode dominates, but the role of the DA-mode decreases with decreasing quenching coefficient. At the highest pressure explored, 50 mTorr, electron heating in the sheath region dominates. However, for the highest quenching coefficient there is some contribution from the DA-mode in the plasma bulk, but this contribution decreases to almost zero, and thus a pure  $\alpha$ -mode is observed for quenching coefficient of 0.001 or smaller. We have demonstrated that the surface quenching coefficient of the singlet metastable molecule  $O_2(a^1\Delta_g)$ , and thus the electrode material, more or less dictates the electronegativity within the discharge and the electron heating mechanism, except at very low operating pressure ( $\sim 10$  mTorr). However, the quenching coefficients, even for the most common electrodes, are not very well known.

#### Acknowledgments

The authors are thankful to Ragnar D. B. Jónsson for assistance with the global model calculations. This work was partially supported by the Icelandic Research Fund Grant No. 163086, the University of Iceland Research Fund, and the Swedish Government Agency for Innovation Systems (VINNOVA) contract no. 2014-04876.

- 
- [1] M. A. Lieberman and V. Godyak, IEEE Transactions on Plasma Science **26**, 955 (1998).
  - [2] G. Gozadinos, D. Vender, M. M. Turner, and M. A. Lieberman, Plasma Sources Science and Technology **10**, 117 (2001).
  - [3] B. P. Wood, Ph.D. thesis, University of California at Berkeley (1991).
  - [4] B. P. Wood, M. A. Lieberman, and A. J. Lichtenberg, IEEE Transactions on Plasma Science **23**, 89 (1995).
  - [5] Y.-X. Liu, Q.-Z. Zhang, W. Jiang, L.-J. Hou, X.-Z. Jiang, W.-Q. Lu, and Y.-N. Wang, Physical Review Letters **107**, 055002 (2011).
  - [6] Y.-X. Liu, Q.-Z. Zhang, J. Liu, Y.-H. Song, A. Bogaerts, and Y.-N. Wang, Applied Physics Letters **101**, 114101 (2012).
  - [7] S. Wilczek, J. Trieschmann, J. Schulze, E. Schüngel, R. P. Brinkmann, A. Derzsi, I. Korolov, Z. Donkó, and T. Mussenbrock, Plasma Sources Science and Technology **24**, 024002 (2015).
  - [8] U. Czarnetzki, T. Mussenbrock, and R. Brinkmann, Physics of Plasmas **13**, 123503 (2006).
  - [9] Z. Donkó, J. Schulze, U. Czarnetzki, and D. Luggenhölscher, Applied Physics Letters **94**, 131501 (2009).
  - [10] E. Schüngel, S. Brandt, Z. Donkó, I. Korolov, A. Derzsi, and J. Schulze, Plasma Sources Science and Technology **24**, 044009 (2015).
  - [11] S. Wilczek, J. Trieschmann, D. Eremin, R. P. Brinkmann, J. Schulze, E. Schüngel, A. Derzsi, I. K. olov, P. Hartmann, Z. Donkó, et al., Physics of Plasmas **23**, 063514 (2016).
  - [12] P. Belenguer and J. Boeuf, Physical Review A **41**, 4447 (1990).
  - [13] J. Schulze, A. Derzsi, K. Dittmann, T. Hemke, J. Meichsner, and Z. Donkó, Physical Review Letters **107**, 275001 (2011).
  - [14] A. Derzsi, E. Schüngel, Z. Donkó, and J. Schulze, Open Chemistry **13**, 346 (2015).
  - [15] D. L. Pulfrey, F. G. M. Hathorn, and L. Young, Journal of the Electrochemical Society **120**, 1529 (1973).
  - [16] Y. Kawai, N. Konishi, J. Watanabe, and T. Ohmi, Applied Physics Letters **64**, 2223 (1994).
  - [17] D. W. Hess, IBM Journal of Research and Development **43**, 127 (1999).
  - [18] D. L. Tolliver, in *VLSI Electronics: Microstructure Science, vol. 8*, edited by N. G. Einspruch and D. M. Brown (Academic Press, Orlando, 1984), pp. 1–24.
  - [19] M. A. Hartney, D. W. Hess, and D. S. Soane, Journal of Vacuum Science and Technology B **7**, 1 (1989).
  - [20] A. Vesel and M. Mozetic, Vacuum **86**, 634 (2012).
  - [21] M. R. Chashmejahanbin, A. Salimi, and A. Ershad Langroudi, International Journal of Adhesion and Adhesives **49**, 44 (2014).
  - [22] A. Vesel and M. Mozetic, Journal of Physics D: Applied Physics **50**, 293001 (2017).
  - [23] J. T. Gudmundsson, I. G. Kouznetsov, K. K. Patel, and M. A. Lieberman, Journal of Physics D: Applied Physics **34**, 1100 (2001).
  - [24] J. T. Gudmundsson and E. G. Thorsteinsson, Plasma Sources Science and Technology **16**, 399 (2007).

- [25] D. A. Toneli, R. S. Pessoa, M. Roberto, and J. T. Gudmundsson, *Journal of Physics D: Applied Physics* **48**, 325202 (2015).
- [26] J. T. Gudmundsson and M. A. Lieberman, *Plasma Sources Science and Technology* **24**, 035016 (2015).
- [27] J. T. Gudmundsson and B. Ventéjou, *Journal of Applied Physics* **118**, 153302 (2015).
- [28] H. Hannesdottir and J. T. Gudmundsson, *Plasma Sources Science and Technology* **25**, 055002 (2016).
- [29] J. T. Gudmundsson and H. Hannesdottir, *AIP Conference Proceedings* **1811**, 120001 (2017).
- [30] H. Hannesdottir and J. T. Gudmundsson, *Journal of Physics D: Applied Physics* **50**, 175201 (2017).
- [31] J. T. Gudmundsson and D. I. Snorrason, *Journal of Applied Physics* **122**, 193302 (2017).
- [32] J. T. Gudmundsson, D. I. Snorrason, and H. Hannesdottir, *Plasma Sources Science and Technology* **27**, 025009 (2018).
- [33] A. Greb, A. R. Gibson, K. Niemi, D. O’Connell, and T. Gans, *Plasma Sources Science and Technology* **24**, 044003 (2015).
- [34] A. Derzsi, T. Laffleur, J.-P. Booth, I. Korolov, and Z. Donkó, *Plasma Sources Science and Technology* **25**, 015004 (2016).
- [35] A. Derzsi, B. Bruneau, A. Gibson, E. Johnson, D. O’Connell, T. Gans, J.-P. Booth, and Z. Donkó, *Plasma Sources Science and Technology* **26**, 034002 (2017).
- [36] A. R. Gibson and T. Gans, *Plasma Sources Science and Technology* **26**, 115007 (2017).
- [37] J. Hammel and J. P. Verboncoeur, *Bulletin of the American Physical Society* **48**, 66 (2003).
- [38] J. P. Verboncoeur, A. B. Langdon, and N. T. Gladd, *Computer Physics Communications* **87**, 199 (1995).
- [39] J. T. Gudmundsson, E. Kawamura, and M. A. Lieberman, *Plasma Sources Science and Technology* **22**, 035011 (2013).
- [40] A. Midey, I. Dotan, and A. A. Viggiano, *Journal of Physical Chemistry A* **113**, 3040 (2008).
- [41] A. J. Lichtenberg, V. Vahedi, M. A. Lieberman, and T. Rognlien, *Journal of Applied Physics* **75**, 2339 (1994).
- [42] C. Birdsall, *IEEE Transactions on Plasma Science* **19**, 65 (1991).
- [43] E. Kawamura, C. K. Birdsall, and V. Vahedi, *Plasma Sources Science and Technology* **9**, 413 (2000).
- [44] C. Nguyen, Master’s thesis, University of California at Berkeley (2006).
- [45] C.-H. Lim, Ph.D. thesis, University of California at Berkeley (2007).
- [46] R. H. Miller and M. R. Combi, *Geophysical Research Letters* **21**, 1735 (1994).
- [47] J. P. Booth and N. Sadeghi, *Journal of Applied Physics* **70**, 611 (1991).
- [48] S. Du, J. Leng, H. Yang, G. Sha, and C. Zhang, *Chinese Journal of Chemical Physics* **24**, 256 (2011).
- [49] R. L. Sharpless and T. G. Slanger, *Journal of Chemical Physics* **91**, 7947 (1989).
- [50] R. J. O’Brien and G. H. Myers, *Journal of Chemical Physics* **53**, 3832 (1970).
- [51] B. Gordiets, C. Ferreira, V. Guerra, J. Loureiro, J. Nahorny, D. Pagnon, M. Touzeau, and M. Vialle, *IEEE Transactions on Plasma Science* **23**, 750 (1995).
- [52] K. Kutasi, V. Guerra, and P. Sá, *Journal of Physics D: Applied Physics* **43**, 175201 (2010).
- [53] A. Greb, K. Niemi, D. O’Connell, and T. Gans, *Applied Physics Letters* **103**, 244101 (2013).
- [54] R. P. Crannage, E. A. Dorko, D. E. Johnson, and P. D. Whitefield, *Chemical Physics* **169**, 267 (1993).
- [55] G. Perram, D. Determan, J. Dorian, B. Lowe, and T. L. Thompson, *Chemical Physics* **162**, 427 (1992).
- [56] R. P. Steer, R. A. Ackerman, and J. N. Pitts, *Journal of Chemical Physics* **51**, 843 (1969).
- [57] S. J. Arnold and E. A. Ogryzlo, *Canadian Journal of Physics* **45**, 2053 (1967).
- [58] I. D. Clark and R. P. Wayne, *Chemical Physics Letters* **3**, 93 (1969).
- [59] T. P. J. Izod and R. P. Wayne, *Proceedings of the Royal Society of London. Series A, Mathematical and Physical Sciences* **308**, 81 (1968).
- [60] A. Leiss, U. Schurath, K. H. Becker, and E. H. Fink, *Journal of Photochemistry* **8**, 211 (1978).
- [61] M. E. Ryskin and B. R. Shub, *Reaction Kinetics and Catalysis Letters* **17**, 41 (1981).
- [62] E. G. Thorsteinsson and J. T. Gudmundsson, *Plasma Sources Science and Technology* **19**, 055008 (2010).
- [63] R. D. B. Jonsson, B.S. project, University of Iceland, Reykjavik, Iceland, <http://hdl.handle.net/1946/29537> (2018).
- [64] D. O’Connell, T. Gans, D. Vender, U. Czarnetzki, and R. Boswell, *Physics of Plasmas* **14**, 034505 (2007).
- [65] S. V. Berezhnoj, C. B. Shin, U. Buddemeier, and I. Kaganovich, *Applied Physics Letters* **77**, 800 (2000).
- [66] H. M. Katsch, T. Sturm, E. Quandt, and H. F. Döbele, *Plasma Sources Science and Technology* **9**, 323 (2000).
- [67] C. Küllig, K. Dittmann, and J. Meichsner, *Plasma Sources Science and Technology* **19**, 065011 (2010).
- [68] K. Kaga, T. Kimura, and K. Ohe, *Japanese Journal of Applied Physics* **40**, 330 (2001).
- [69] S. Kechkar, P. Swift, S. Kelly, S. Kumar, S. Daniels, and M. Turner, *Plasma Sources Science and Technology* **25**, 065009 (2017).
- [70] G.-H. Liu, Y.-X. Liu, D.-Q. Wen, and Y.-N. Wang, *Plasma Sources Science and Technology* **24**, 034006 (2015).